JACS
JOURNAL OF THE AMERICAN CHEMICAL SOCIETY
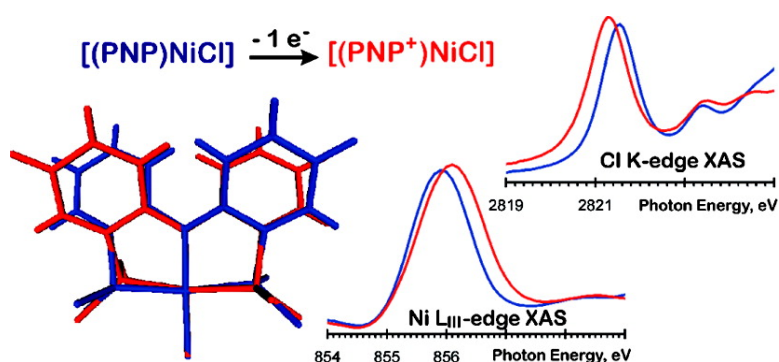
Article

Structural, Spectroscopic, and Theoretical Elucidation of a Redox-Active Pincer-Type Ancillary Applied in Catalysis

Debashis Adhikari, Susanne Mossin, Falguni Basuli, John C. Huffman, Robert K. Szilagyi, Karsten Meyer, and Daniel J. Mindiola

More About This Article

Additional resources and features associated with this article are available within the HTML version:

- Supporting Information
- Links to the 6 articles that cite this article, as of the time of this article download
- Access to high resolution figures
- Links to articles and content related to this article
- Copyright permission to reproduce figures and/or text from this article

View the Full Text HTML

ACS Publications
High quality. High impact.

Structural, Spectroscopic, and Theoretical Elucidation of a Redox-Active Pincer-Type Ancillary Applied in Catalysis

Debashis Adhikari,[†] Susanne Mossin,[‡] Falguni Basuli,[§] John C. Huffman,[†]
Robert K. Szilagyi,*[,‖] Karsten Meyer,[‡] and Daniel J. Mindiola*[,†]

*Department of Chemistry and the Molecular Structure Center, Indiana University, Bloomington,
Indiana 47405, Inorganic Chemistry, Friedrich-Alexander University Erlangen-Nuremberg,
Egerlandstrasse 1, Erlangen, Germany 91058, and Department of Chemistry and Biochemistry,
Montana State University, Bozeman, Montana 59717*

Received December 10, 2007; E-mail: szilagyi@montana.edu; mindiola@indiana.edu

Abstract: Pincer-type ligands are believed to be very robust scaffolds that can support multifarious functionalities as well as highly reactive metal motifs applied in organometallic chemistry, especially in the realm of catalysis. In this paper, we describe the redox and, therefore, noninnocent behavior of a PNP (PNP⁻ = N[2-P(CHMe₂)₂-4-methylphenyl]₂) pincer ancillary bound to nickel. A combination of structural, spectroscopic, and theoretical techniques suggests that this type of framework can house an electron hole when coordinated to Ni(II).

1. Introduction

Pincer-type ligands are an archetypical support for unsaturated transition metals as well as systems possessing reactive functional groups often applied in catalysis.[1] These supporting skeletons are exclusively chosen given their robustness and ability to stabilize the metal ion without facile decomplexation.[1] In the theme of organometallic chemistry, complexes supported by these scaffold types are capable of promoting C—X bond breaking and making events applicable to polymerization,[2] cross-coupling,[3] and functionalization reactions (where X = H, C, O, N, and the halides) among a myriad of other important transformations.[4] When using late metals, the latter transformations can be often accompanied by important redox events such as oxidative addition/reductive elimination steps. Recent studies, however, have demonstrated that certain ligands, when combined with electron-rich metal centers, can behave as electron reservoirs, and that such a property can be imperative along

the bond forming event.[5] To date, pincer ligands invoking the protoypical PXP (X = C and N) coordination sphere have not been thoroughly investigated in terms of their role as noninnocent ligands.[6] This is especially true since they lack the intuitively obvious redox-active functional groups such as quinone and thioquinones.[7] Herein, we present compelling evidence to suggest that the pincer ligand PNP (PNP⁻ = N[2-P(CHMe₂)₂-4-methylphenyl]₂),[8] a common ancillary support applied to organometallic chemistry, can operate as a redox-active site. Structural, spectroscopic (UV−vis, EPR, multiedge XAS), and theoretical analysis of a Ni(II) and its Ni(II) radical cation counterpart reveal the N and aryl fragments of the ligand, for the latter species, to house the radical hole when such a framework is exposed to a one-electron oxidant.

2. Results and Discussion

2.1. Synthesis and Solid-State Structure of Complex 1 and its Radical Cation [1][OTf]. Our pincer framework can be readily incorporated onto Ni(II) to form the square-planar complex (PNP)NiCl (**1**).[8,9] To gain insight into the oxidation potential of **1**, we performed a cyclic voltammetry experiment

---

† Indiana University.
‡ Friedrich-Alexander University Erlangen-Nuremberg.
§ Current address: Nuclear Medicine; Brigham and Women's Hospital, Harvard Medical School, Boston, Massachusetts 02115.
‖ Montana State University.

(1) (a) van der Boom, M. E.; Milstein, D. *Chem. Rev.* **2003**, *103*, 1759−92. (b) Milstein, D. *Pure Appl. Chem.* **2003**, *75*, 445−60. (c) Vigalok, A.; Milstein, D. *Acc. Chem. Res.* **2001**, *34*, 798−807. (d) Morales-Morales, D.; Jensen, C. M. *The Chemistry of Pincer Compounds*, 1st ed.; Elsevier: Oxford, 2007.
(2) Gossage, R. A.; van de Kuil, L. A.; van Koten, G. *Acc. Chem. Res.* **1998**, *31*, 423−31.
(3) (a) Fan, L.; Ozerov, O. V. *Chem. Commun.* **2005**, *35*, 4450−2. (b) Jones, G. D.; Martin, J. L.; McFarland, C.; Allen, O. R.; Hall, R. E.; Haley, A. D.; Brandon, R. J.; Konovalova, T.; Desrochers, P. J.; Pulay, P.; Vicic, D. A. *J. Am. Chem. Soc.* **2006**, *128*, 13175−83.
(4) (a) Zhao, J.; Goldman, A. S.; Hartwig, J. F. *Science* **2005**, *307*, 1080−82. (b) Ghosh, R.; Zhang, X.; Achord, P.; Emge, T. J.; Krogh-Jespersen, K.; Goldman, A. S. *J. Am. Chem. Soc.* **2007**, *129*, 853−66. (c) Zhang, X.; Emge, T. J.; Ghosh, R.; Goldman, A. S. *J. Am. Chem. Soc.* **2005**, *127*, 8250−51.

(5) (a) Scott, J.; Gambarotta, S.; Korobkov, I.; Budzelaar, P. H. M. *Organometallics* **2005**, *24*, 6298−300. (b) Bart, S. C.; Chlopek, K.; Bill, E.; Bouwkamp, M. W.; Lobkovsky, E.; Neese, F.; Wieghardt, K.; Chirik, P. J. *J. Am. Chem. Soc.* **2006**, *128*, 13901−12. (c) Vidyaratne, I.; Scott, J.; Gambarotta, S.; Budzelaar, P. H. M. *Inorg. Chem.* **2007**, *46*, 7040−49. (d) Knijnenburg, Q.; Hetterscheid, D.; Kooistra, T. M.; Budzelaar, P. H. M. *Eur. J. Inorg. Chem.* **2004**, 1204−11.
(6) Frech, C. M.; Ben-David, Y.; Weiner, L.; Milstein, D. *J. Am. Chem. Soc.* **2006**, *128*, 7128−9.
(7) (a) Ray, K.; Bill, E.; Weyhermueller, T.; Wieghardt, K. *J. Am. Chem. Soc.* **2005**, *127*, 5641−54. (b) Haneling, M. R.; Heyduk, A. F. *J. Am. Chem. Soc.* **2006**, *128*, 8410−1.
(8) (a) Weng, W.; Yang, L.; Foxman, B. M.; Ozerov, O. V. *Organometallics* **2004**, *23*, 4700−5. (b) Ozerov, O. V.; Guo, C.; Papkov, V. A.; Foxman, B. M. *J. Am. Chem. Soc.* **2004**, *126*, 4792−3. (c) Fan, L.; Foxman, B. M.; Ozerov, O. V. *Organometallics* **2004**, *23*, 326−8.
(9) Ozerov, O. V.; Guo, C.; Fan, L.; Foxman, B. M. *Organometallics* **2004**, *23*, 5573−80.
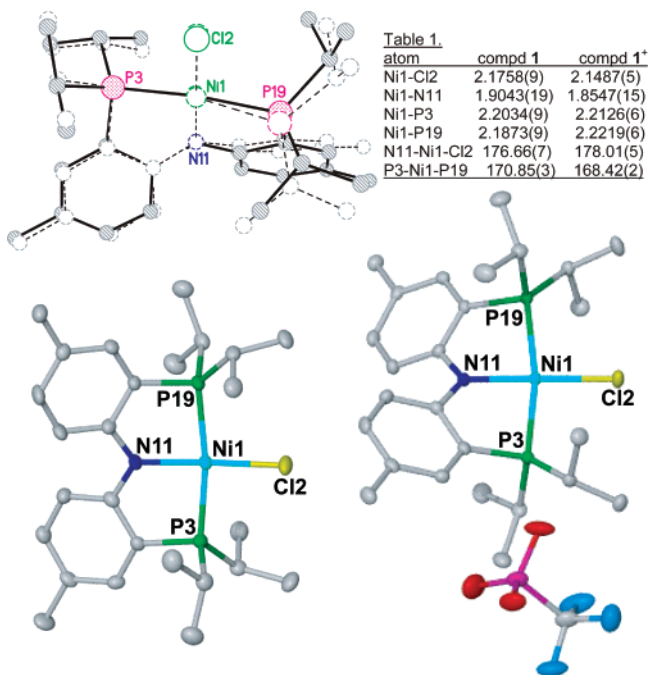
Figure 1. Least-squares fit of **1** (solid line) and **1**⁺ (dashed line) omitting hydrogens, solvent (in **1**), and anion (in [**1**][OTf]). The atoms Ni, P, P, N, Cl, and bridging phenyl carbons are fitted (top left). Weighted rms deviation = 0.0695 Å. Selected distances in Table 1 are reported in angstroms and angles in degrees (top right). Bottom figures represent the solid-state structure for **1** (left) and [**1**][OTf] (right) displaying thermal ellipsoids at the 50% probability level. Hydrogen atoms and one THF (for **1**) have been omitted for the purpose of clarity.

Table 1. atom	compd 1	compd 1⁺
Ni1-Cl2	2.1758(9)	2.1487(5)
Ni1-N11	1.9043(19)	1.8547(15)
Ni1-P3	2.2034(9)	2.2126(6)
Ni1-P19	2.1873(9)	2.2219(6)
N11-Ni1-Cl2	176.66(7)	178.01(5)
P3-Ni1-P19	170.85(3)	168.42(2)

and observed a reversible anodic wave at −0.06 V versus Fc⁺/Fc⁰ at 0.00 V.[10] Chemical oxidation of **1** with [Fc][OTf] evinced a rapid color change from green to purple, and extraction of the more soluble Fc from the reaction mixture with pentane afforded crude salt [**1**][OTf], which can be crystallized as dark purple needles in 87% yield (eq 1).
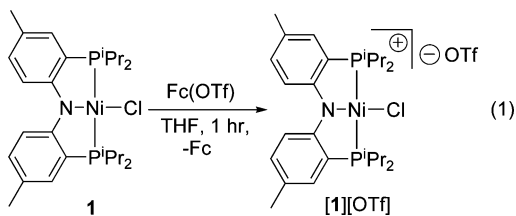
To establish the connectivity of the paramagnetic compound, [**1**][OTf], we relied on single-crystal X-ray structural data (XRD).[11−13] The geometry of the resulting complex was scrutinized to be a cationic and square-planar nickel system bearing an essentially "noninteractive" triflate group (Figure 1). Although the dihedral angles defined by the atoms Ni−P−C_{aryl}−C_{aryl} slightly differ between [**1**][OTf] and the XRD of its neutral counterpart, **1**, further inspection of other metrical parameters

reveal very similar structural features between these molecules (Figure 1), thus implying that oxidation of the metal center has not taken place. On the basis of this observation, it would seem logical to assume that the redox event took place at the ligand PNP scaffold, but the similarity in alternating C−C bond lengths in both solid-state structures of **1** and [**1**][OTf] are too contiguous to assign the new ligand as a quinoid-type short−long−short altering sequence of C−C bonds in the rings.[14]

2.2. Solution and Solid-State X-Band EPR Spectra for Complex [1][OTf]. As expected, solution-state magnetization measurements by the Evans method are consistent with complex [**1**][OTf] being a radical (μ_{eff} = 2.21(1) μ_B), and we therefore turned our attention to X-band EPR spectroscopy to investigate the radical nature of [**1**][OTf]. Accordingly, the room temperature solution X-band EPR spectrum of [**1**][OTf] in CH_2Cl_2/toluene (Figure 2) revealed an isotropic signal at g_{iso} = 2.0238(3). The g-value is close to the free electron value of 2.0023 proving the electron hole to be mainly ligand localized, since average g-values for Ni(III) are typically found in the range 2.15−2.20.[15,16] Moreover, the spectrum displays resolved superhyperfine structure originating from interaction of the unpaired spin with the nitrogen, the two phosphorus atoms, and the six aromatic hydrogens composing the pincer ligand, which further substantiates our claim of a ligand PNP radical cation to be present in [**1**][OTf] (Figure 2). Using the crystal structure of [**1**][OTf] as a starting point, a model was constructed for the nuclei expected to contribute to the overall super-hyperfine structure. Intuitively, this model contains the ligating nitrogen atom and the two aromatic hydrogens on carbons of the PNP support, which are ortho with respect to the amide, since these are expected to contribute the largest spin density. To explain the number of lines observed in the solution X-band EPR spectrum of [**1**][OTf], it was necessary to also include contributions from the two phosphorus atoms as well as the four meta aromatic hydrogens. Although the phosphorus atoms should have a low percentage of spin density according to the DFT calculation (vide infra), the high nuclear g_n value for phosphorus (2.263) often makes super-hyperfine coupling observable regardless. Despite the chlorine atom having a nuclear spin of ³/₂ for both common isotopes (³⁵Cl, 76%; ³⁷Cl, 24%), super-hyperfine coupling to chloride is commonly not observed due to the low nuclear g_n value of around 0.5 for both isotopes.[17] Given the observed line widths, super-hyperfine coupling to chloride is not likely to be resolved here.[18] An inflection point is observed in the experimental spectrum in accordance with the one N, two P's, two H's, and four H's model outlined here. The isotropic simulation shown in red was performed using: S = ¹/₂, g_{iso} = 2.0238(3), line width 0.31 mT, Gaussian line shape; hyperfine coupling to one nitrogen, I = 1, 0.97 mT; two hydrogens and two phosphorus, I = ¹/₂, 0.76 mT and I = ¹/₂, 0.50 mT; and four hydrogens I = ¹/₂, 0.33 mT. At this stage,

(10) Adhikari, D.; Mossin, S.; Basuli, F.; Chipara, M.; Fan, H.; Huffman, J. C.; Baik, M.-H.; Meyer, K.; Mindiola, D. J. Manuscript submitted for publication.

(11) See Supporting Information.

(12) Single crystals of **1** grown from Et₂O produce a nonsolvent polymorph to that for structure of **1·THF**. The structural parameters for each polymorph are virtually identical.

(13) Relatively similar structures to complex **1** have been reported using the PNP analogues N(o-C₆H₄PR₂)₂⁻ (R = Ph, ⁱPr). Liang, L.-C.; Chien, P.-S.; Lin, J.-M.; Huang, M.-H.; Huang, Y.-L.; Liao, J.-H. *Organometallics* **2006**, *25*, 1399−411.

(14) (a) Alves, H.; Simao, D.; Novais, H.; Santos, I. C.; Gimenez-Saiz, C.; Gama, V.; Waerenborgh, J. C.; Henriques, R. T.; Almeida, M. *Polyhedron* **2003**, *22*, 2481−6. (b) Sellmann, D.; Geck, M.; Knoch, F.; Ritter, G.; Dengler, J. *J. Am. Chem. Soc.* **1991**, *113*, 3819−28. (c) Collins, T. J.; Powell, R. D.; Slebodnick, C.; Uffelman, E. S. *J. Am. Chem. Soc.* **1991**, *113*, 8419−25.

(15) Shimazaki, Y.; Tani, F.; Fukui, K.; Naruta, Y.; Yamauchi, O. *J. Am. Chem. Soc.* **2003**, *125*, 10512−3.

(16) Lovecchio, F.; Gore, E.; Busch, D. *J. Am. Chem. Soc.* **1974**, *96*, 3109−18.

(17) Nipales, N. S.; Westmoreland, T. D. *Inorg. Chem.* **1995**, *34*, 3374−7.

(18) Bemtgen, J.-M.; Gimpert, H.-M.; von Zelewsky, A. *Inorg. Chem.* **1983**, *22*, 3576−80.
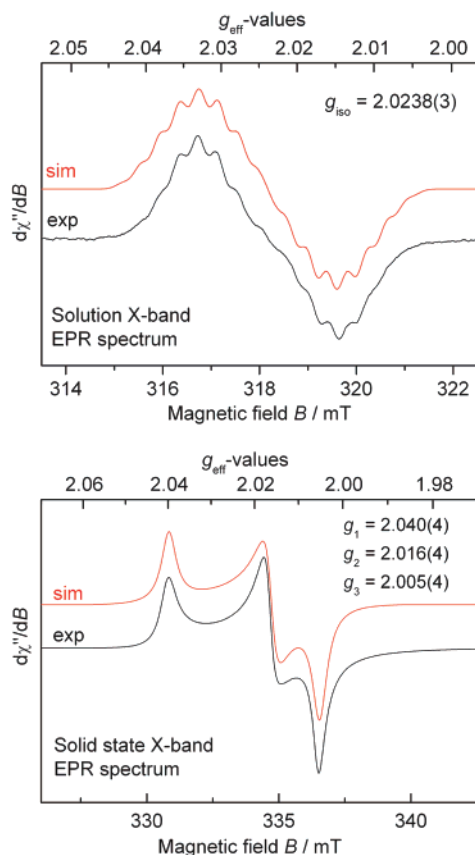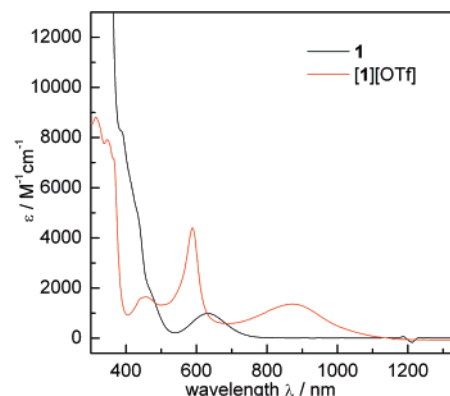
Figure 3. UV−vis spectra of **1** and [**1**][OTf], stacked together to show the changing features.

<500 nm. For [**1**][OTf], three absorption bands at 872 (ϵ = 1359 M^{-1} cm^{-1}), 589 nm (ϵ = 4293 M^{-1} cm^{-1}), and 443 (ϵ = 1606 M^{-1} cm^{-1}) are clearly observed (Figure 3). While the latter two can be ascribed to a high-intensity charge-transfer band (MLCT), the near-infrared (NIR) band could be the result of a low energy $\pi^*\leftarrow\pi$ transition.[7a,14] The transition observed at 872 nm is consistent with a lower aromatic π/π^* orbitals due to the increase in the effective nuclear charge of the ligand atoms and in accord with oxidation of this scaffold.[7a,19] Near-IR transitions of this type have been suggested to be valuable spectroscopic markers for noninnocent ligands.[14] Multiedge X-ray absorption spectroscopy will be consistent with the aforementioned description (vide infra).

2.4. Multiedge X-ray Absorption Spectroscopic Data for 1 and [1][OTf]. A direct experimental way of probing ligand-based redox chemistry is to study the redox-active orbitals by multiedge X-ray absorption spectroscopic (XAS) technique.[20] We carried out XAS measurements at Ni L-, Cl K-, and P K-edges to determine changes in the electronic structure upon oxidation of **1** to [**1**][OTf]. The Ni L_{III}-edge spectrum of **1** (red trace in Figure 4A) displays an intense feature at ∼855.9 eV with a less intense feature at ∼860.3 eV. The latter feature is absent for the $NiCl_2$ spectrum (control reference, black line). Upon consideration of the frontier molecular orbitals, the first (pre-edge at ∼856 eV) absorption peak can be assigned to an excitation of the Ni core 2p electrons into the lowest unoccupied orbital (LUMO). The approximate 1.6 eV higher feature in **1** relative to $NiCl_2$ is indicative of a larger energy separation between the donor Ni 2p and acceptor LUMO orbitals. Such a deviation could be due to different ligand field splitting in the Ni(II) ions (i.e., octahedral in oligomeric $NiCl_2$ and square-planar in **1**) that would shift the energy of the acceptor orbital. In addition, a greater Ni effective nuclear charge in **1** can lower the energy of the Ni 2p orbital that results in shifting the XAS features to higher energy. The multiedge approach allows for dissecting these effects from the experimental data. Examination of the Cl K-edge spectra in Figure 4B shows features between 2820 and 2824 eV that are proportional to the amount of chloride character in the LUMO orbital.[20] Since the intensities and the rising-edge energy positions at 2826.6 eV are comparable in both $NiCl_2$ (black trace) and **1** (red trace), it can be concluded

Figure 2. The top part depicts the solution EPR spectrum recorded at 292 K of [**1**][OTf] in CH_2Cl_2 (0.3 mM) with a microwave frequency of 9.013244 GHz, microwave power 8 mW, and modulation width of 0.03 mT. The spectrum was collected over multiple runs. The bottom figure displays the solid-state X-band EPR spectrum of [**1**][OTf] recorded at 292 K with a microwave frequency of 9.445896 GHz, microwave power 1 mW, and modulation width 0.1 mT. Modulation frequency was 100 kHz in both spectra. The red lines display simulations performed with the parameters given in the text.

the coupling constants cannot be assigned between the two phosphorus atoms and the two ortho hydrogens, since they both have $I = {}^1/_2$. Due to the line width, uncertainties are large for both H and P coupling constants (0.1 mT) but much less so for the nitrogen super-hyperfine coupling constant which has a direct influence on the overall shape of the derivative signal observed.

When the room-temperature X-band EPR spectrum of a solid sample of [**1**][OTf] is recorded, a rhombic signal is observed (Figure 2). The simulation shown in red was performed with $S = {}^1/_2$, and g_1, g_2, g_3 equal to 2.040(4), 2.016(4), and 2.005(4), respectively. The average of these values matches the isotropic g-value observed in solution, hence consistent with [**1**][OTf] being the origin of these two signals. The anisotropy in the g-values observed in the solid state originates from nickel(III) and implies that a non-negligible amount of spin density should also be present at the nickel center.[15] This is also manifested by the significant increase in the isotropic g-value in solution compared to the free electron value: $\Delta g = g_{iso} - g_e = 0.0215$-(3), and is also consistent with the theoretical DFT calculations (vide infra).

2.3. Absorption Spectra for 1 and [1][OTf]. An absorption spectrum of [**1**][OTf] in CH_2Cl_2 exhibits distinguishably separate features from its neutral parent component **1**, which shows a band at 636 (ϵ = 685 M^{-1} cm^{-1}) as well as shoulders at energies

(19) (a) Sellmann, D.; Binder, H.; Haussinger, D.; Heinemann, F. W. *Inorg. Chim. Acta* **2000**, *300−302*, 829−36. (b) Carrasco, R.; Cano, J.; Otten-waelder, X.; Aukauloo, A.; Journaux, Y.; Ruiz-Garcia, R. *Dalton Trans.* **2005**, *15*, 2527−38.
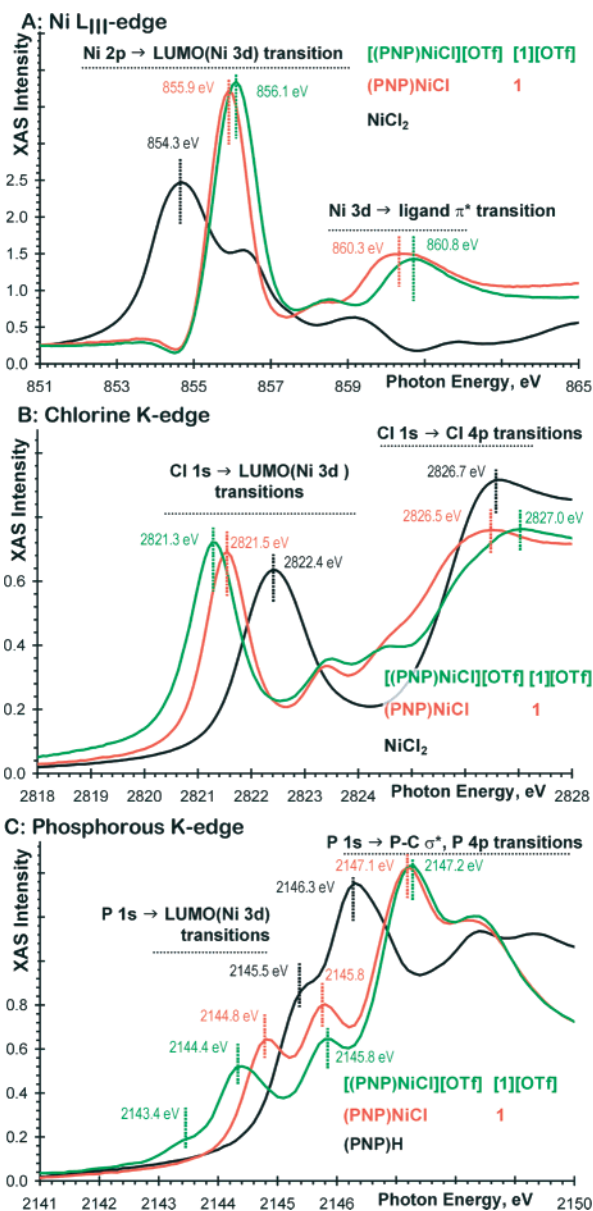(20) Boysen, R. B.; Szilagyi, R. K. *Inorg. Chim. Acta* (http://dx.doi.org/10.1016/j.ica.2007.07.032).

Figure 4. Multiedge XAS spectra of reference compounds and complexes **1** and [**1**][OTf], having as reference NiCl₂ and (PNP)H.

that the Cl 3p→Ni 3d electron donation, i.e., Ni−Cl bond covalency, should be comparable as well. This feature suggests that the effective nuclear charges of the Cl⁻ ligands are also similar. The higher energy Cl K-edge pre-edge feature at ∼2822.4 eV in Figure 4B and the lower energy Ni L-edge pre-edge feature at ∼854.3 eV in Figure 4A indicate a higher lying Ni 2p orbital in NiCl₂ versus **1** (2821.5 and 855.9 eV, respectively). This translates into a greater Ni effective nuclear charge in **1** due to back-donation from the Ni to the PNP ligand that shows up at the Ni L$_{III}$-edge as a higher energy feature at ∼860 eV (Figure 4A). These similar higher energy features show up at the Ni L$_{II}$-edge for **1**, with comparable relative intensities to the pre-edge peak, thus implying that these excitations are Ni-based. Furthermore, a recent study by Solomon et al. has also described these higher lying, intense features as experimental evidence for metal-to-ligand back-bonding.[21]

Most notably, comparison of the Ni L$_{III}$-edge spectra of **1** and [**1**][OTf] reveal only subtle changes upon one-electron

oxidation, which is a direct evidence that the redox process only affects the metal to a limited extent (Figure 4A). For example, the 0.2 eV shift in the pre-edge feature is negligible when compared to the 1−2 eV shift per electron redox change for nickel-based redox processes reported in the literature.[22] In a comparison of the Cl K-edge of **1** to [**1**][OTf] (Figure 4B, red vs green lines), it is apparent that the Cl⁻ covalency (thus donation) increased in [**1**][OTf] relative to **1**, since the slightly more intense pre-edge peak at ∼2821.3 eV is shifted to lower energies and the rising edge positions are shifted to higher energies by ∼0.5 eV in [**1**][OTf] (green trace) relative to **1** (red trace). Since we did not observe a significant change in the metal oxidation state from Figure 4A, the Cl⁻ must be donating directly to ligand-based orbitals and not to the metal.

In order to directly assess the role of the phosphines in [**1**]-[OTf], we also obtained data at the P K-edge (Figure 4C). For comparison, the spectrum of free (PNP)H ligand is shown as reference (black line) with two intense low-energy features at 2145.5 and 2146.3 eV, and these can be assigned to P core 1s electron transitions into the aromatic and the two aliphatic P−C σ* orbitals. Since the aliphatic P−C bonds are unaffected by redox changes, we can use these as internal references for estimating the P effective nuclear charge. As a result, ligand complexation to Ni promotes a +0.9 eV shift in these features; which is due to the electron donation from the P lone pair into the vacant metal 3d/4s/4p-orbitals. The slight increase in the separation of the aromatic (2145.8 eV) and aliphatic (2147.2 eV) P−C σ* transitions relative to the free ligand is indicative of changes in the electronic structure of the aromatic moiety of the phosphine ligand. The oxidation of the PNP ligand is expected to lower the aromatic π/π* orbitals due to the increase of the effective nuclear charge of the ligand atoms which is consistent with changes observed for the absorption spectrum for [**1**][OTf] (vide supra). More importantly, the appearance of a new pre-edge feature at 2144.8 eV in **1** relative to the free ligand is due to the Ni 3d−P 3p covalent interaction in the LUMO (Figure 5). Upon oxidation, a shoulder appears at 2143.4 eV in [**1**][OTf], which corresponds to a rather small P 3p character in the SOMO. The energy shift of −0.4 eV of the transitions related to the LUMO of **1** (2144.8 eV) and [**1**][OTf] (2144.4 eV) are due to the increase in the PNP ligand effective nuclear charge, which results in an overall energy decrease of the LUMO orbital. A similar trend has been described for chloride[23] and thiolate[24] complexes with first row di- and trivalent transition metals. Thus, from our Ni L-edge data (Figure 4A) we have determined that the metal center in question is only slightly redox active, and that the radical charge must be confined within the diarylamido residue, more specifically, at the N atom and carbon atoms of the PNP ligand.

In order to corroborate the above interpretation of the multiedge XAS data with the molecular orbital picture, we performed electronic structure calculations to ascertain the HOMO/LUMO orbital compositions for both **1** and **1**⁺.[11] Figure 5A,B depicts the redox-active orbitals of **1** as well as their

(21) Hocking, R. K.; Wasinger, E. C.; deGroot, F. M. F.; Hodgson, K. O.; Hedman, B.; Solomon, E. I. *J. Am. Chem. Soc.* **2006**, *128*, 10442−51.
(22) Wang, H.; Ge, P.; Riordan, C. G.; Brooker, S.; Woomer, C. G.; Collins, T.; Melendres, C. A.; Graudejus, O.; Bartlett, N.; Cramer, S. P. *J. Phys. Chem. B* **1998**, *102*, 8343−6.
(23) Shadle, S. E.; Hedman, B.; Hodgson, K. O.; Solomon, E. I. *J. Am. Chem. Soc.* **1995**, *117*, 2259−72.
(24) Williams, K. R.; Hedman, B.; Hodgson, K. O.; Solomon, E. I. *Inorg. Chim. Acta* **1997**, *263*, 315−21.
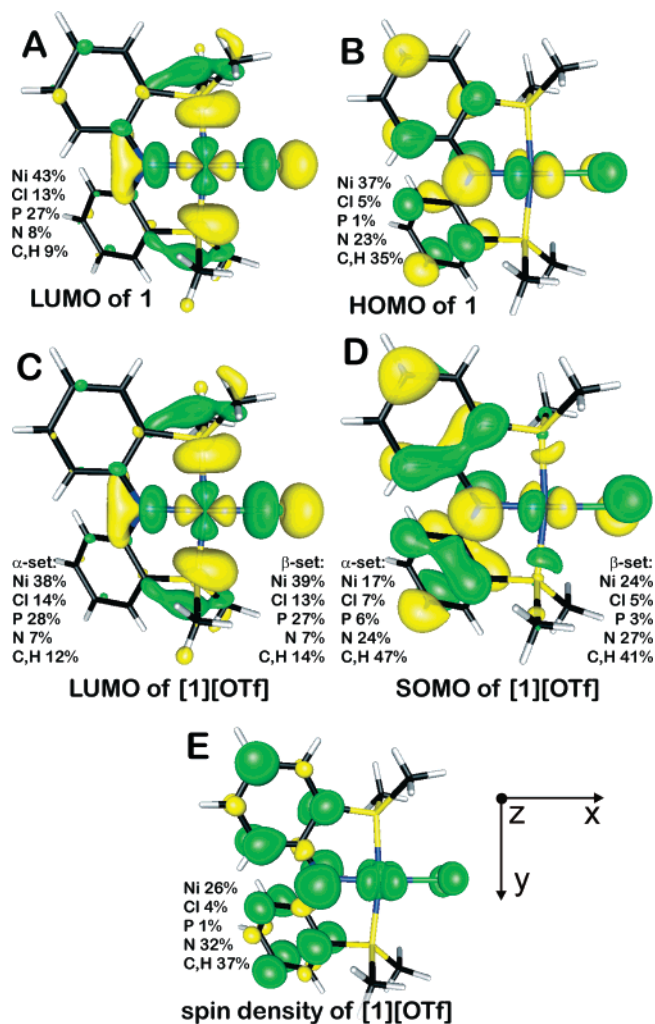
Figure 5. Frontier molecular orbitals of a simplified model of **1** (iPr and tolyl methyl groups have been replaced by hydrogen atoms), and the SOMO orbital and atomic spin density plot for **1**+ calculated using BP86 functional and BSV in Amsterdam Density Functional package.

atomic compositions that were directly probed by our XAS measurements. As expected for a square-planar Ni(II) complex, the LUMO is a combination of the Ni $3d_{x^2-y^2}$ orbital with approximately equal contributions from the chloride and each phosphorus 3p orbitals. In the LUMO orbital, the PNP ligand's involvement is limited to the in-plane (*xy* plane) amido N lone pair, with only a fractional amount of C character due to skewing of the aryl motifs. However, the HOMO orbital shows considerably greater PNP character (59%) that involves an out-of-plane amido N $2p_z$ lone pair and aromatic carbon $2p_z$ contributions. Consequently, the metal $3d_{xz}$ and chloride $3p_z$ orbital contributions are reduced relative to the LUMO, and the perpendicular nature of the HOMO (along the *z*-axis) forbids the phosphorus atoms from contributing significantly to the overall orbital picture.

Logically, oxidation of **1** will generate an electron hole in the HOMO, and the orbital composition of the HOMO already predicts that a ∼59% PNP ligand-based oxidation process should occur. However, one must take into consideration that the oxidation will prompt considerable electron relaxation due to the change in the effective nuclear charge of the atoms as described experimentally by changes in the rising-edge positions in Figure 4C. Such a feature will reorganize the orbital

contributions to eventually decrease in metal character to 17−24% per electron hole in the SOMO of **1**+ (Figure 5D) versus the 37% contribution in the HOMO of **1** (Figure 5A). In addition, the chlorine and phosphorus character increases by a few fractions of a percent, which is consistent with the data shown in Figure 4B,C, respectively. Furthermore, the contribution of the aromatic ring of PNP increases the most by ∼15%, indirectly indicating that one-electron oxidation in **1** affects this component of the complex the most. As observed experimentally in the Ni L-edge and Cl K-edge pre-edge intensities in Figure 4 as well as the calculated orbital contributions in **1** versus [**1**]-[OTf], the LUMO coefficients (Figure 5A,C) remain the same within 5% upon one-electron oxidation. Likewise, the atomic spin densities for [**1**][OTf] indicate small contributions of 26%, 4%, and 1% for Ni, Cl, and P centers, respectively (bottom of Figure 5E). In contrast, the dominant feature of the spin density is located on the amido N (31%) and C (38%) residues of the PNP ligand, which corroborates well with our room-temperature X-band EPR spectrum and orbital analysis (Figure 2, vide supra).

3. Conclusions

In conclusion, applying a wide range of characterization methods such as XRD, EPR, UV−vis, and multiedge XAS in combination with DFT analysis of the orbitals and spin densities, we have characterized a square-planar Ni(II) radical cation complex where the electron hole resides mostly at the nitrogen and aryl carbon atoms (ortho and para positions) of the pincer-type PNP ligand. This observation is especially significant since aminyl radicals (or amine radical cations) are considered short-lived intermediates and play important roles in both chemical and biological transformations.[25] Wieghardt and co-workers have reported aminyl radical complexes of Co and Mn,[26a] while Grützmacher and co-workers have reported a trop2N aminyl radical coordinated to a cationic Rh center (where the trop in question is 5*H*-dibenzo[*a,d*]cycloheptene-5-yl).[26b] Interaction of the unpaired electron with aryl hydrogens and phosphorus was also established spectroscopically by EPR, but this interaction is considered "weak" on the basis of the coupling constant along with atomic spin density distribution from our DFT analysis. With our studies, this type of robust framework, often applied in organometallic chemistry and catalysis, can now be added to the list of noninnocent ligand types.[27] The ability of PNP to house an electron hole provides credible proof that redox processes such as oxidative additions or reductive eliminations involving PNP-supported nickel complexes (e.g., Ni(0)/Ni(II), Ni(II)/Ni(IV) couples) could be transpiring via a stepwise process whereby the ligand peripheral motif might be partially housing a radical along the two-electron sequence (e.g., a Ni(I) radical anion and a Ni(III) radical cation). Multiedge X-ray absorption spectroscopy that provides ground-state, electronic structural information about both metal and ligand contributions

(25) (a) Penkert, F. N.; Weyhermuller, T.; Bill, E.; Hildebrandt, P.; Lecomte, S.; Wieghardt, K. *J. Am. Chem. Soc.* **2000**, *122*, 9663−73. (b) Büttner, T.; Geier, J.; Frison, G.; Harmer, J.; Calle, C.; Schweiger, A.; Schönberg, H.; Grützmacher, H. *Science* **2005**, *307*, 235−8.
(26) (a) Esker, J. L.; Newcomb, M. *Adv. Heterocycl. Chem.* **1993**, *58*, 1−45. (b) Stubbe, J.; van der Donk, W. A. *Chem. Rev.* **1998**, *98*, 705−62.
(27) NCN and PCP bis-pincer-type ligands have been recently reported to be noninnocent supports for dinuclear Ru centers. Gagliardo, M.; Amijs, C. H. M.; Lutz, M.; Spek, A. L.; Havenith, R. W. A.; Hartl, F.; van Klink, G. P. M.; van Koten, G. *Inorg. Chem.* **2007**, *46*, 11133−44.

to the redox-active orbitals is a powerful technique since it can identify noninnocent behavior, and, therefore, predict ligand-based reactivity.

4. Experimental Section

4.1. General Procedures. Unless otherwise stated, all operations were performed in an M. Braun Lab Master double-dry box under an atmosphere of purified nitrogen or using high vacuum standard Schlenk techniques under an argon atmosphere.[28] Anhydrous *n*-hexane, pentane, toluene, and benzene were purchased from Aldrich in sure-sealed reservoirs (18 L) and dried by passage through two columns of activated alumina and a Q-5 column.[29] Diethyl ether was dried by passage through a column of activated alumina.[29] THF was distilled, under nitrogen, from purple sodium benzophenone ketyl and stored under sodium metal. Distilled THF was transferred under vacuum into a thick walled reaction vessel before being transferred into a drybox. C_6D_6 was purchased from Cambridge Isotope Laboratory (CIL), degassed, and vacuum transferred to 4 Å molecular sieves. Celite, alumina, and 4 Å molecular sieves were activated under vacuum overnight at 200 °C. Li(PNP) (PNP = N[2-P(CHMe$_2$)$_2$-4-methylphenyl]$_2$$^-$)[8] and (PNP)NiCl[8,9] were prepared according to the literature. [Fc][OTf] was prepared by addition of an equalmolar amount of AgOTf to recrystallized Fc (FeCp$_2$) in THF. Removal of Ag^0 and concentrating and cooling of the filtrate to -35 °C afforded dark blue needles of [Fc][OTf], which were collected, washed with Et$_2$O, and dried under reduced pressure (>90% yield). All other chemicals were used as received. CHN analyses were performed by Desert Analytics, Tucson, AZ. ^{1}H spectra were recorded on Varian 400 or 300 MHz NMR spectrometers. ^{1}H is reported with reference to solvent resonances (residual proteo solvent in CD$_2$Cl$_2$, 5.32 ppm). Solution magnetization measurements were determined by the method of Evans.[30,31] UV$-$vis spectra were recorded on a Cary 5000 UV$-$vis$-$NIR spectrophotometer.

4.2. Single-Crystal X-ray Diffraction Details. X-ray diffraction data were collected on a SMART6000 (Bruker) system under a stream of N$_2$ (g) at low temperatures.[32,33] Single crystals of **1** (THF) and [**1**][OTf] (CH$_2$Cl$_2$ layered with hexane) were grown at -35 °C and room temperature, respectively, from concentrated solutions. Inert-atmosphere techniques were used to place the crystal onto the tip of a diameter glass capillary (0.10 mm) mounted on a SMART6000 (Bruker) at 128$-$132(2) K. A preliminary set of cell constants was calculated from reflections obtained from three nearly orthogonal sets of 30 frames. The data collection was carried out using graphite-monochromated Mo Kα radiation with a frame time of 5$-$20 s and a detector distance of 5.0 cm. A randomly oriented region of a sphere in reciprocal space was surveyed. In general, three sections of 606 frames were collected with 0.30° steps in ω at different ϕ settings with the detector set at $-43°$ in 2θ. Final cell constants were calculated from the xyz centroids of strong reflections from the actual data collection after integration (SAINT).[32] The structure was solved using SHELXS-97 and refined with SHELXL-97.[33] A direct-methods solution was calculated which provided most non-hydrogen atoms from the E-map. Full-matrix least-squares/difference Fourier cycles were performed, which located the remaining non-hydrogen atoms. All non-hydrogen atoms were refined with anisotropic displacement parameters. All hydrogen atoms were located in subsequent Fourier maps and included as isotropic contributors in the final cycles of refinement.

Crystal data for **1**·THF follow: C$_{30}$H$_{48}$ClNNiOP$_2$, M_w = 594.79 g/mol, monoclinic, space group $P2_1/c$, a = 19.183(6) Å, b = 11.709-(4) Å, c = 14.676(3) Å, β = 110.738(8)°, Z = 4, μ = 0.843 mm^{-1}, Mo Kα = 0.71073 Å, V = 3082.8(17) Å^3, T = 128(2), ρ_{calcd} = 1.282 mg/mm^3, GOF on F^2 = 0.820, R1 = 3.34% and wR2 = 6.95% (F^2, all data). Out of a total of 11398 reflections collected 6112 were unique, and 4205 were observed (R_{int} = 3.75%) with $I > 2\sigma I$ (dark green cleaved cube, 0.18 × 0.15 × 0.15 mm^3, 27.49° ≥ θ ≥ 2.08°). A disordered THF solvent is present and was modeled as two distinct molecules. All (non-THF) hydrogen atoms were located in subsequent Fourier maps and included as isotropic contributors in the final cycles of refinement.

Crystal data for [**1**][OTf] follow: C$_{27}$H$_{40}$ClF$_3$NNiO$_3$P$_2$S, M_w = 671.76 g/mol, monoclinic, space group $P2_1/n$, a = 10.9057(9) Å, b = 18.8042(15) Å, c = 14.7900(11) Å, β = 92.510(2)°, Z = 4, μ = 0.951 mm^{-1}, Mo Kα = 0.71073 Å, V = 3030.1(4) Å^3, T = 132(2), ρ_{calcd} = 1.473 mg/mm^3, GOF on F^2 = 0.806, R1 = 3.38% and wR2 = 6.80% (F^2, all data). Out of a total of 27480 reflections collected, 8843 were unique, and 5686 were observed (R_{int} = 5.99%) with $I > 2\sigma I$ (dark green cleaved cube, 0.25 × 0.12 × 0.10 mm^3, 30.01° ≥ θ ≥ 2.16°).

4.3. X-Band EPR Details. The EPR measurements were performed in quartz tubes with young valves. Solid-state X-band EPR spectra were recorded in a Bruker EMX EPR instrument. Anisotropic simulation was performed using the program ESRSIM written by Høgni Weihe, University of Copenhagen, Denmark.[34] Solution EPR spectra were recorded on a JEOL continuous wave spectrometer JES-FA200 equipped with an X-band Gunn oscillator bridge, a cylindrical mode cavity, and a helium cryostat. The *g*-value in the solution spectrum was calibrated using the second and fourth line of the Mn^{2+} hyperfine spectrum from an external Mn marker. The marker consists of Mn^{2+} thermally dispersed in MgO placed on the tip of a probe which is inserted slightly into the cavity. The cavity was tuned with both sample and probe inserted. The Mn marker is provided with the JEOL JES-FA200 spectrometer. The isotropic simulation was performed using the JEOL Isotropic Simulation program ISOSimu/FA version 2.1.0.

4.4. XAS Details. The nickel L-, phosphorus K-, and chlorine K-edge XAS measurements were carried out at beamlines 10-1 and 6-2 of Stanford Synchrotron Radiation Laboratory under strorage ring (SPEAR 3) conditions of 3 GeV energy and 100$-$80 mA beam current. BL10-1 has a 30-pole 1.45 T Wiggler insertion device with a 6 m spherical grating monochromator. The samples were measured in a vacuum chamber with typical pressures of 10^{-6}$-$10^{-8} Torr, and the energy was scanned between 820 and 980 eV. The incident beam intensity and beam line optics were optimized at 860 eV. The energy scale was calibrated to the L$_{III}$ and L$_{II}$ edges of NiF$_2$ at 854.7 and 871.9 eV. Data collection was carried out in electron yield mode by a Channeltron detector with 1.5kV accelerating potential. BL6-2 is a 56-pole, 0.9 T Wiggler beam line with a liquid nitrogen cooled, Si(111) double crystal monochromator. P and Cl K-edge spectra were collected in the energy ranges 2120$-$2320 and 2720$-$3050 eV, respectively, using an unfocused beam in a He-purged fly path at room temperature and a three-grid Lytle fluorescence detector. The beam line was optimized at 2320 and 3050 eV at the P and Cl K-edge, respectively. The energy scale was calibrated to the most intense feature of OPPh$_3$ at 2147.5 eV and for the Cl K-edge at 2820.2 eV using the pre-edge feature of Cs$_2$CuCl$_4$. The solid samples were ground and pasted onto a contaminant free Kapton tape from Shercon or carbon tape from Specs CertiPrep in a glove box with sub-ppm oxygen and moisture levels. For the P and Cl K-edge measurements, samples were protected by a thin polypropylene window (Specs CertiPrep) from exposure to air during sample mounting and change. Sample holders for Ni L-edge measurements were mounted in a He purged glove bag tightly wrapped around the vacuum chamber. The incident photon energy was scanned in 0.5 eV steps outside the

(28) For a general description of the equipment and techniques used in carrying out this chemistry, see: Burger, B. J.; Bercaw, J. E. In *Experimental Organometallic Chemistry*; Wayda, A. L., Darensbourg, M. Y., Eds.; ACS Symposium Series 357; American Chemical Society: Washington, DC, 1987; pp 79$-$98.

(29) Pangborn, A. B.; Giardello, M. A.; Grubbs, R. H.; Rosen, R. K.; Timmers, F. J. *Organometallics* **1996**, *15*, 1518$-$20.

(30) Sur, S. K. *J. Mag. Reson.* **1989**, *82*, 169$-$73.

(31) Evans, D. F. *J. Chem. Soc.* **1959**, 2003$-$5.

(32) *SAINT 6.1*; Bruker Analytical X-Ray Systems: Madison, WI, 1999.

(33) *SHELXTL-Plus V5.10*; Bruker Analytical X-Ray Systems: Madison, WI, 1998.

(34) Jacobsen, C. J. H.; Pedersen, E.; Villadsen, J.; Weihe, H. *Inorg. Chem.* **1993**, *32*, 1216$-$21.

rising edge region where the step size was 0.1 eV. At least five scans were averaged to obtain a good signal-to-noise ratio. Further processing of the data has been carried out as described in the literature.[21,35]

4.5. Preparation of [(PNP)NiCl][OTf], [1][OTf]. In a vial, (PNP)-NiCl, **1** (100 mg, 0.191 mmol), was taken in 5 mL THF and the solution cooled to −35 °C. An analogously cold solution/suspension of [Fc]-[OTf] (62.72 mg, 0.187 mmol) was added dropwise to **1** and the mixture stirred for 1 h. The solution color changes to deep purple immediately upon addition of [Fc][OTf]. After the completion of the reaction, the solution was dried under vacuo, and the residue was washed three times (∼5 mL each time) with pentane to extract the byproduct, ferrocene (Fc), which was confirmed by ^{1}H NMR spectroscopy. Dark purple crystals of [**1**][OTf] were obtained from the mixture at −35 °C (112 mg, 0.166 mmol, 87% yield) from a CH_2Cl_2 (∼3 mL) layered solution with hexane (2 full pipettes) over 5 days. ^{1}H NMR (25 °C, 399.8 MHz, CD_2Cl_2): δ 7.35 (br, $\Delta\nu_{1/2}$ = 6 Hz), 7.21 (br, $\Delta\nu_{1/2}$ = 34 Hz), 3.68 (br, $\Delta\nu_{1/2}$ = 21 Hz), 3.45 (br, $\Delta\nu_{1/2}$ = 24 Hz), 2.34 (br, $\Delta\nu_{1/2}$ = 15 Hz), 1.15 (br, $\Delta\nu_{1/2}$ = 20 Hz). μ_{eff} : 2.21(1) μ_B (CD_2Cl_2, 25 °C, Evans method). UV−vis−NIR (CH_2Cl_2, 25 °C) 443 nm (ϵ = 1606 M^{-1} cm^{-1}), 589 nm (ϵ = 4293 M^{-1} cm^{-1}), 872 nm (ϵ = 1359 M^{-1} cm^{-1}). Anal. Calcd for $C_{27}H_{40}NClF_3NiO_3P_2S$: C, 48.28; H, 6.00; N 2.09. Found: C, 47.90; H, 5.82, N, 2.02. Mp 220(2) °C.

4.6. Electronic Structure Calculations. Density functional calculations were carried out using the Amsterdam Density Functional package.[36] The electronic structures of the computational models [(PNP)NiCl] (**1**) and [(PNP)NiCl][OTf] ([**1**][OTf]) were calculated by employing a gradient corrected density functional composed of Becke nonlocal and Slater local density functional exchange[37a] and Perdew nonlocal and Vosko−Wilk−Nussair local density functional correlation[37b] functions (BP or BP86). Calculations were carried out using a triple-ζ basis set with double polarization function (TZ2P or BSIV in ADF).

The structures of the computational model were derived from their crystal structures without any modification and are provided as Supporting Information. The molecular orbital diagrams and spin density plots were generated using the GOpenMol[38] visualizer program.

Supporting Information Available: Complete crystallographic data, structure, solution, and refinement of the complexes (**1**·THF, a polymorph of **1**·THF, and [**1**][OTf]), and Cartesian coordinates of the simplified computational models. This material is available free of charge via the Internet at http://pubs.acs.org.

JA7108486

(35) Solomon, E. I.; Hedman, B.; Hodgson, K. O.; Dey, A.; Szilagyi, R. K., *Coord. Chem. Rev.* **2005**, *249*, 97−129.
(36) Velde, G. T.; Bickelhaupt, F. M.; Baerends, E. J.; Guerra, C. F.; Van Gisbergen, S. J. A.; Snijders, J. G.; Ziegler, T. *J. Comput. Chem.* **2001**, *22*, 931−67.
(37) (a) Becke, A. D. *Phys. Rev. A: Gen. Phys.* **1988**, *38*, 3098−100. (b) Perdew, J. P. *Phys. Rev. B: Condens. Mater.* **1986**, *33*, 8822−4.
(38) (a) Laaksonen, L. *J. Mol. Graph.* **1992**, *10*, 33−4. (a) Bergman, D. L.; Laaksonen, L.; Laaksonen, A. *J. Mol. Graph. Model.* **1997**, *15*, 301−6.